



HAL
open science

Structure–property relationships in normal and mixed dithienylethenes – polyoxometalates supramolecular assemblies with fast solid-state photochromic properties

Oleh Stetsiuk, Patricia Bolle, Marie Cordier, Julien Boixel, Rémi Dessapt

► To cite this version:

Oleh Stetsiuk, Patricia Bolle, Marie Cordier, Julien Boixel, Rémi Dessapt. Structure–property relationships in normal and mixed dithienylethenes – polyoxometalates supramolecular assemblies with fast solid-state photochromic properties. *Journal of Materials Chemistry C*, 2022, 10 (3), pp.899-907. 10.1039/D1TC04561J . hal-03475124

HAL Id: hal-03475124

<https://univ-rennes.hal.science/hal-03475124>

Submitted on 3 Feb 2022

HAL is a multi-disciplinary open access archive for the deposit and dissemination of scientific research documents, whether they are published or not. The documents may come from teaching and research institutions in France or abroad, or from public or private research centers.

L'archive ouverte pluridisciplinaire **HAL**, est destinée au dépôt et à la diffusion de documents scientifiques de niveau recherche, publiés ou non, émanant des établissements d'enseignement et de recherche français ou étrangers, des laboratoires publics ou privés.



Distributed under a Creative Commons Attribution - NonCommercial 4.0 International License

Structure-property relationships in normal and mixed dithienylethenes – polyoxometalates supramolecular assemblies with fast solid-state photochromic properties

Received 00th January 20xx,
Accepted 00th January 20xx

DOI: 10.1039/x0xx00000x

Oleh Stetsiuk,^{ab} Patricia Bolle,^b Marie Cordier,^a Julien Boixel^{*a} and Rémi Dessapt^{*b}

Five new highly photochromic hybrid organic-inorganic materials were successfully prepared by supramolecular assembly of normal (**1**⁺) and mixed (**2**⁺) cationic dithienylethenes (DTEs) and polyoxometalates (POMs) units. Single-crystal X-ray diffraction studies reveal that (1)₃[PM₁₂O₄₀]-5ACN (M = W, Mo) (**1-PW**₁₂ and **1-PMo**₁₂) and (2)₃[PM₁₂O₄₀]-5ACN (M = W, Mo) (**2-PW**₁₂ and **2-PMo**₁₂) are isostructural, while (2)₄[Mo₈O₂₆]-4DMF (**2-Mo**₈) is an isotype of (1)₄[Mo₈O₂₆]-4DMF (**1-Mo**₈) i.e., the first POM-DTE ionic assembly, recently reported. The solid-state photochromic properties of these materials at room temperature are highly tunable with the nature of the DTEs and POMs used, which has been interpreted taking into account steric and electronic factors. Especially, while **1-PMo**₁₂ and **2-PMo**₁₂ exhibit negligible photoresponses which have not been considered herein, thorough investigations of the photocoloration and fading kinetics in ambient conditions have highlighted the precise impact of both organic and inorganic components on the photoswitching abilities of **1-Mo**₈, **2-Mo**₈, **1-PW**₁₂ and **2-PW**₁₂. Upon UV-light irradiation, the absorption of the normal and mixed DTEs in their closed-ring form exhibits a hypsochromic shift which is more pronounced in hybrid systems integrating β-[Mo₈O₂₆]⁴⁻ rather than α-[PW₁₂O₄₀]³⁻, due to the higher negative charge density of the octamolybdate unit. The photocyclization rates of DTEs are also systematically increased when combined with the β-[Mo₈O₂₆]⁴⁻ unit, while in contrast, their back cycloreversion rates are not affected whatever the nature of the POMs used. In addition, within isostructural series, hybrids integrating mixed DTEs exhibit faster fading processes than their normal DTE counterparts when exposed to visible light. Finally, among this new series, **2-Mo**₈ shows the best photochromic performances with a fast photocoloration rate associated with a high coloration contrast, a fast and complete fading process and a high cyclability.

Introduction

Polyoxometalates are a unique class of redox and optically active metal-oxide anionic clusters which have been widely studied in many domains including catalysis,^{1, 2} biology,^{3, 4} magnetism,⁵ optics,^{6, 7} and materials sciences.^{8, 9} Among all investigated POMs materials, hybrid organic-inorganic polyoxometalates (hybrid-POMs) are designed to combine the intrinsic properties of the distinct molecular subunits into optimized devices for synergistic effects and new applications.¹⁰ In the field of photochromic materials, the hybrid-POM systems have been at first built by ionic assembling of POMs and organoammonium cations (OACs).^{11, 10, 12} Their photochromic behavior in the solid state, which is based on the photoreduction of the POM units assisted by H-atom transfer from OACs,^{11, 12} has proven its efficiency in many fields with applications such as ultraviolet sensors,¹³ sustainable

materials,^{14, 15} catalysis,² and memory devices,^{16, 17} taking advantage of the contactless and energy tunable properties of light. Another class of photochromic supramolecular hybrid-POMs has been later designed where OACs are replaced by organosulfonium cations (OSCs). In these systems, the mechanism of photocoloration does not require direct H-bonding interactions between the POMs and the organic cations.¹⁸

Instant color change upon photoirradiation along the photochromic cycle is generally a sought-after feature in these domains, and more particularly for optical data storage application that requires rapid “ON – OFF” states. While fast photocoloration rates have been raised in various optimized hybrid-POM systems, large improvements are still needed to accelerate and enhance the fading process. For this purpose, changing the common OAC (or OSC) cations by another organic part with intrinsic photochromic properties, is a promising alternative strategy. Following this concept, several photoactive hybrid materials incorporating spiropyrans or spirooxazines photochromic units covalently^{7, 19-21} or ionically^{22, 23} assembled with POMs have been already reported. This coupling allows improving the thermal stability of the organic switches, and finely directing their photoisomerization in the solid state.

To go further in designing efficient solid-state photoswitches with faster photoresponses and improved cyclabilities,

^aUniv Rennes, CNRS, ISCR – UMR6226, F-35000, Rennes, France

^bUniversité de Nantes, CNRS, Institut des Matériaux Jean Rouxel, IMN, F-44000 Nantes, France

E-mails: remi.dessapt@cnrs-imn.fr and julien.boixel@univ-rennes1.fr

Electronic Supplementary Information (ESI) available: Detailed syntheses, ¹H, ¹⁹F and ¹³C, ESI-HRMS, FT-IR, UV-vis spectra, X-ray crystallographic data, TGA measurements. CCDC 2057188-2057193. For ESI and crystallographic data in CIF or other electronic format see DOI: 10.1039/x0xx00000x

dithienylethenes (DTE)-based systems are particularly attractive given their well-adapted photochromic features of DTEs gathering rapid and reversible photoswitching reactions together with thermally stable open and closed-ring isomers in solution and in the solid state, as well as remarkable photofatigue resistance.²⁴ Moreover, their two forms exhibit distinct electronic and optical characteristics highly tunable by rational design, which has motivated their use for the photoswitching of numerous properties, such as luminescence,^{21, 25} conductivity,^{26, 27} nonlinear optics,^{28, 29} magnetism,³⁰ and catalytic ability.³¹ Considering the potential of coupling DTE photochromes with POMs, we recently designed (1)₄[Mo₈O₂₆]-4DMF (**1-Mo₈**) which is the first ionic assembly of an asymmetrical methylpyridinium DTE cation (**1⁺**) (Scheme 1) and a β-[Mo₈O₂₆]⁴⁻ unit.³² The POM unit modifies the solid-state photoresponse of **1⁺** via both steric and electronic effects, resulting in a considerable blue-shift of almost 50 nm in its closed form absorption band, while maintaining the efficiency of its almost complete and fast photocyclization process, as well as its good cyclability. In order to deeper understand the synergic processes between POMs and DTEs during photoirradiation, and to improve further the fading rate and the photofatigue resistance of such supramolecular assemblies, we investigate another type of DTE called “mixed” formed with one 3-methyl-thiophene and one 2-methyl-thiophene, while “normal” DTE backbones bear two 3-methyl-thiophene. Although mixed DTEs have been much less studied than their normal analogues, it has been shown that their quantum yields of photo-cycloreversion reaction are significantly higher than the ones of normal DTEs, leading to faster and complete reopening reaction in solution.³³ We thus envision to take advantage of this specific feature, and transfer the photoswitching efficiency of mixed DTEs from the solution to the solid state, through supramolecular assembling with POMs. We report herein the straightforward preparation and photophysical investigations of five new POM-DTE ionic assemblies. We sequentially changed the organic (DTE) and inorganic (POM) components in order to performed a step-by-step photophysical investigation, and to establish a detailed comparison on their optical properties. Based on our previous study, we firstly modified the nature of the DTE and successfully synthesized the new (2)₄[Mo₈O₂₆]-4DMF (**2-Mo₈**) assembly, an isotype of **1-Mo₈**, where **2⁺** is a new asymmetrical methylpyridinium-containing mixed DTE cation (Scheme 1). Secondly, four new DTE-POM systems have been prepared, namely (1)₃[PM₁₂O₄₀]-5ACN (M = W, Mo) (**1-PW₁₂** and **1-PMo₁₂**) and (2)₃[PM₁₂O₄₀]-5ACN (M = W, Mo) (**2-PW₁₂** and **2-PMo₁₂**), where the DTE is either a normal type (**1⁺**) or a mixed type (**2⁺**), associated with the well-known Keggin-type POM. Single-crystal X-ray diffraction studies revealed that all these assemblies are isostructural. The thorough investigation of their solid-state photochromic properties at room temperature gives fine understanding on synergistic effects between DTE (normal vs mixed) and POM (molybdenate vs tungstenate) components.

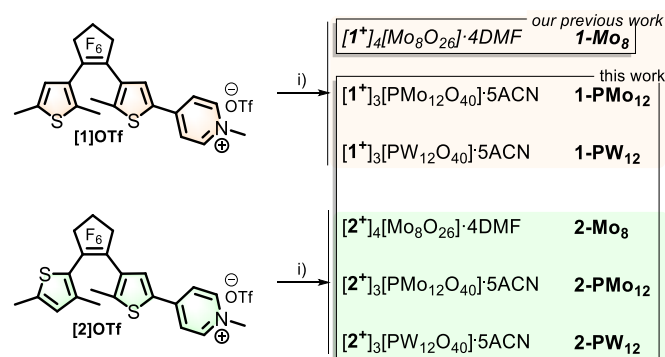
Results and discussion

Synthesis and characterization of [2]OTf and the five DTE-POM assemblies

Synthesis

[**1**]OTf has been prepared following our reported procedure. The triflate salts of the second targeted cationic DTE [**2**]OTf have been obtained by the treatment of the corresponding new neutral pyridyl DTE **2**, with an excess of methyl triflate in dry CH₂Cl₂ solution (Scheme 1).³⁴ **2** was obtained through an adapted procedure, by replacing the 3-bromo-2,5-dimethylthiophene precursor by the 2-bromo-3,5-dimethylthiophene (Fig. S1, ESI⁺).^{35, 36} The purity of **2** and [**2**]OTf has been confirmed by means of ¹H, ¹³C, ¹⁹F NMR spectroscopies (Fig. S2 and S3, ESI⁺), mass spectrometry (Fig. S2 and S4, ESI⁺), FT-IR spectroscopy (Fig. S5, ESI⁺), and elemental analysis (ESI⁺).

Single-crystals of the DTE-POM assemblies have been obtained by mixing in dry acetonitrile (ACN) or in DMF a stoichiometric amount of a cationic DTE ([**1**]OTf or [**2**]OTf) with the tetrabutylammonium salts of the considered POM anions (NBu₄)₄[α-Mo₈O₂₆] or (NBu₄)₃[α-PM₁₂O₄₀] (M = W or Mo) (Scheme 1), following the procedure recently reported by our group.³² The presence of positively charged sp² pyridyl-N-atom in [**1**]OTf and [**2**]OTf favored the electrostatic assemblies with the POMs in comparison with the starting tetrabutylammonium cation, due to the shielded sp³ positive charge by the alkyl-chains. The composition and purity of the obtained hybrid materials have been further confirmed by FT-IR spectroscopy (Fig. S6-S8, ESI⁺) and elemental analysis (ESI⁺). The IR spectrum of **2-Mo₈** shows the Mo=O and Mo-O-Mo vibration modes of the β-[Mo₈O₂₆]⁴⁻ anion in the range 1000-400 cm⁻¹, associated with the vibrational signature of **2⁺** and DMF molecules in the range of 1650-1000 cm⁻¹ (Fig. S6, ESI⁺). The IR spectra of the tungstenate (**1-PW₁₂**, **2-PW₁₂**) and molybdenate (**1-PMo₁₂**, **2-PMo₁₂**) series show similar features with four characteristic bands at 1078, 979, 895, 810 cm⁻¹ and 1060, 956, 878 and 800 cm⁻¹, respectively, which correspond to ν(P-O), ν(M-O_{terminal}), ν(M-O_a-M octahedral corner-sharing) and ν(M-O_b-M octahedral edge-sharing) vibrational modes (Fig. S7 and S8, ESI⁺).^{32, 37, 38} The absence of splitting of the ν(M-O_a-M) band well characterizes the α-isomer of the Keggin-type anions.



Scheme 1 Synthetic routes for the targeted POM/DTE assemblies from normal (**1⁺**) and mixed (**2⁺**) DTE cations. i) (NBu₄)₄[α-Mo₈O₂₆] or (NBu₄)₃[α-PM₁₂O₄₀] (M = W, Mo), CH₃CN or DMF.

Crystal structures

Both **2** and **[2]OTf** crystallize in the monoclinic system $P2_1/c$ space group (Table S1, ESI[†]), with one independent DTE in its open form (respectively labeled as **2o** and **2o***) in the unit cell. The thienyl groups of both molecules adopt a photoactive antiparallel conformation (Fig. 1a and S9, ESI[†]). The distances between the two reactive carbon atoms are 3.592(2) and 3.643(4) Å for **2** and **[2]OTf**, respectively (Tables S2 and S3, ESI[†]), slightly shorter than that observed for **[1]OTf** (3.687(33) Å),³² which indicates that they are close enough to undergo photocyclization reaction. The unit cells of **2** and **[2]OTf** (Fig. 1b and Fig. S9 and S10, ESI[†]) are additionally stabilized with numerous intermolecular H-bonds between the fluorine atoms of the bridge and the hydrogen atoms of both the methyl groups and the pyridinium ring, as detailed in Table 1 and Table S4, ESI[†].

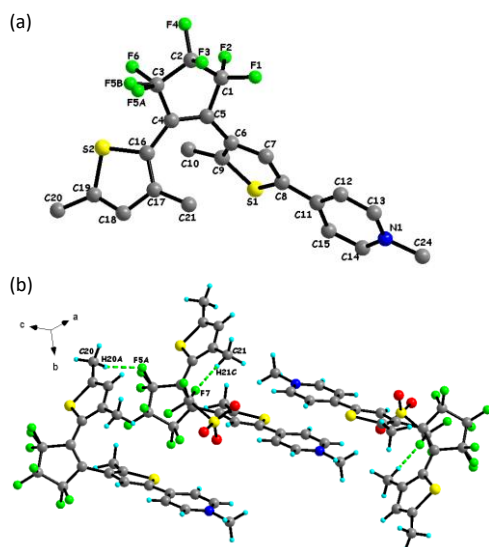


Fig. 1 Crystal structure of **[2]OTf**. (a) Structure of **2o*** with atom labelling. (b) Stacking of the **2o*** and triflate molecules with intermolecular H-bonds (green dotted lines).

Table 1 Distances and angles values of the intermolecular H-bonds in **[2]OTf**.

$d(\text{F}\cdots\text{H})$ [Å]	$d(\text{A}\cdots\text{D})$ [Å]	$\angle(\text{AHD})$ [°]
$\text{F}(5\text{A})\cdots\text{H}(20\text{A}) = 2.3788(55)$	$\text{C}(20)\cdots\text{F}(5\text{A}) = 3.3162(71)$	160
$\text{F}(7)\cdots\text{H}(21\text{C}) = 2.6377(35)$	$\text{C}(21)\cdots\text{F}(7) = 3.5913(55)$	164

2-Mo₈ crystallizes in the triclinic system (Table S1, ESI[†]). Its unit cell shows a β -[Mo₈O₂₆]⁴⁻ anion, two crystallographically independent **2⁺** cations in their open form and two crystallized DMF molecules as independent fragments (Fig. 2a). The **2⁺** molecules are in their photoactive antiparallel conformation, and the distances between the two reactive carbon atoms (3.550(15) and 3.607(12) Å) are slightly shorter than that observed for **[2]OTf** (3.643(4) Å). Noticeably, the crystal packing of **2-Mo₈** is similar to that previously observed for **1-Mo₈**,³² as a consequence of very comparable structures for the **1⁺** and **2⁺** molecules (Scheme 1). The octamolybdate block is surrounded by four **2⁺** cations whom the aromatic pyridinium rings are involved in the formation of additional $\pi\cdots\pi$ interactions with the oxygen POM facets, the shortest distances being of about 2.95 Å (Fig. 2b and Fig. S11, ESI[†]). One of the two DMF

molecules involves $\pi\cdots\pi$ interactions with the pyridinium ring of one **2⁺** unit, with a short O \cdots N distance of 3.062(9) Å, while the second DMF molecule forms no significant interaction.

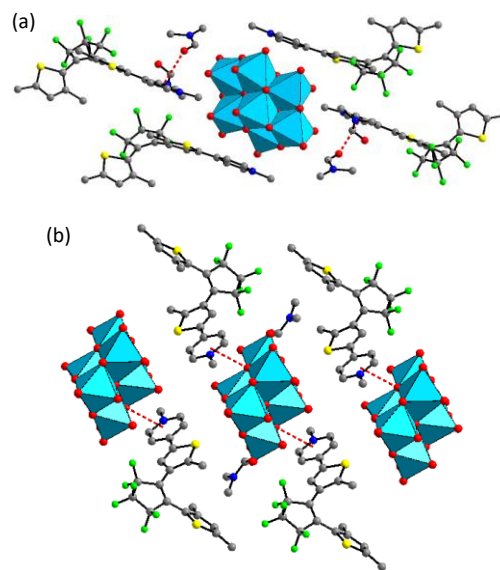


Fig. 2 (a) Crystal structure of **2-Mo₈**. The red dotted lines illustrate $\pi\cdots\pi$ interactions between DMF molecules and the pyridinium ring of **2⁺**. (b) Crystal packing of **2-Mo₈** showing the $\pi\cdots\pi$ interactions (red dotted lines) between oxygen POM facets and the pyridinium ring of **2⁺** (blue octahedra: MoO₆, red sphere: oxygen, yellow sphere: sulfur, blue sphere: nitrogen, green sphere: fluorine, grey sphere: carbon). H atoms were omitted for clarity.

The four **1-PM₁₂** and **2-PM₁₂** (M = Mo, W) compounds are all isostructural and crystallize in the triclinic system (Table S1, ESI[†]). Their unit cells show one entire α -[PM₁₂O₄₀]³⁻ anion, three cationic DTE molecules and non-coordinated ACN molecules (Fig. 3 and Fig. S12, ESI[†]). Attempts to obtain single-crystals of **1-PW₁₂** suitable for X-ray diffraction analysis were unsuccessful, and its structure is not reported herein. The number of ACN molecules in **2-PW₁₂**, **2-PMo₁₂** and **1-PMo₁₂** could not be precisely determined directly from X-ray diffraction data. The residual electron densities were squeezed with Platon, and the total number of electrons per unit cell is in a good agreement with the TGA and elemental analyses, therefore resulted in five crystallized ACN molecules. The structure of **2-PW₁₂** has been chosen herein to describe the crystal packing in this series, and detailed structures of **1-PMo₁₂** and **2-PMo₁₂** are presented in Fig. S12-S16, ESI[†] for comparison.

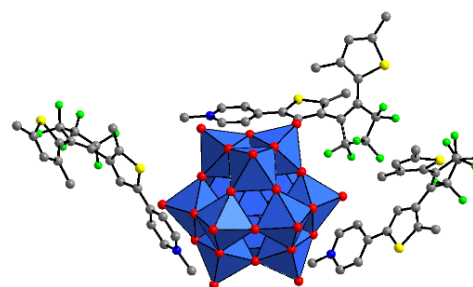


Fig. 3 Crystal structure of **2-PW₁₂**. The α -[PW₁₂O₄₀]³⁻ anion is represented in polyhedral mode (blue octahedra: WO₆, orange tetrahedron: PO₄, red sphere: oxygen, yellow sphere: sulfur, blue sphere: nitrogen, green sphere: fluorine, grey sphere: carbon). H atoms and acetonitrile molecules were omitted for clarity.

The three DTE units are in their open forms and exhibit suitable photoactive metrics with antiparallel conformations and typical C...C distances between the two reactive carbon atoms (Fig. 3 and Table 2). In the unit cell, the bulky α -[PW₁₂O₄₀]³⁻ anions are surrounded by the pyridinium rings of the DTEs (Fig. 4 and Fig. S12-S17, ESI⁺). Numerous π ... π interactions between the oxygen-POM facets and the cationic heterocycles are observed, with oxygen-to-centroid distances ranging from 3.08 to 3.27 Å (Table 2). These distances are comparable with those observed in **2-Mo₈** (3.34 Å) and in **1-Mo₈** (3.38 Å).

Table 2 Comparison of the C...C distances between the reactive carbon atoms of DTEs, and π ... π interactions (oxygen-to-centroid) distances around the α -[PM₁₂O₄₀]³⁻ anions in **1-PMo₁₂**, **2-PMo₁₂**, and **2-PW₁₂**.

	C...C distances [Å]	π ... π interactions distances [Å]
1-PMo₁₂	3.561(12); 3.566(19); 3.70(9)	3.08; 3.15; 3.22
2-PMo₁₂	3.627(18); 3.63(2); 3.88(3)	3.11; 3.17; 3.20
2-PW₁₂	3.64(3); 3.65(2); 3.88(3)	3.13; 3.22; 3.27

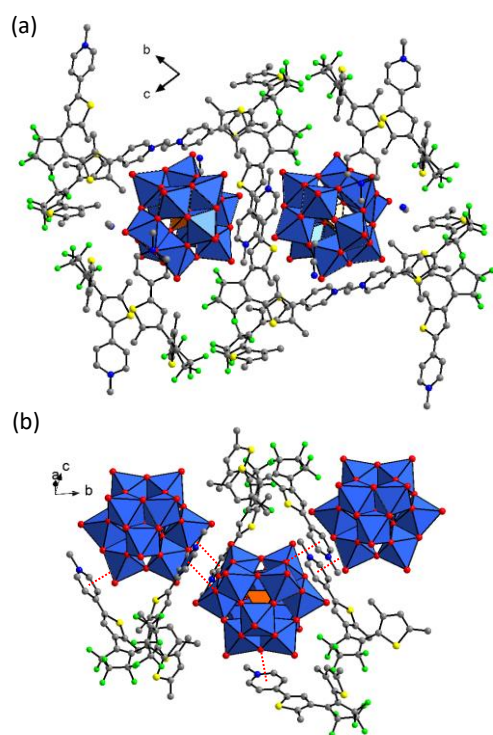


Fig. 4 (a) Unit cell of **2-PW₁₂** along the a-axis. (b) Crystal packing of **2-PW₁₂** showing the π ... π interactions (red dotted lines) between oxygen POM facets and pyridinium rings (blue octahedra: WO₆, orange tetrahedron: PO₄, red sphere: oxygen, yellow sphere: sulfur, blue sphere: nitrogen, green sphere: fluorine, grey sphere: carbon). H atoms were omitted for clarity.

Thermogravimetric analysis

The thermal behaviors of **1-PMo₁₂**, **1-PW₁₂**, **2-PMo₁₂** and **2-PW₁₂** have been examined by thermogravimetric analysis, performed under N₂/O₂ atmosphere. All the recorded thermograms exhibit similar trends, and that of **2-PMo₁₂** is described as an example (Fig. S18, ESI⁺). The first weight loss (5.26 %) appears from 20–185°C, that corresponds to five non-coordinated ACN molecules (theoretical weight loss of 5.94 %). A second broad weight loss (42.30 %) occurs

at ca. 240–650°C, which corresponds to the gradual decomposition of the three cationic DTEs (theoretical weight loss of 41.22 %).

Photochromic properties

Photochromism of **2** and **[2]OTf** in solution

The photochromic properties in CH₂Cl₂ solution of both **2** and **[2]OTf** have been monitored by UV-visible absorption and ¹H NMR spectroscopies. 350 and 525 nm light irradiations are used to trigger the photocyclization and the back cycloreversion reactions, respectively. The electronic absorption spectra of **2** and **[2]OTf** are presented in Fig. 5, and the related data are summarized in Table 3.

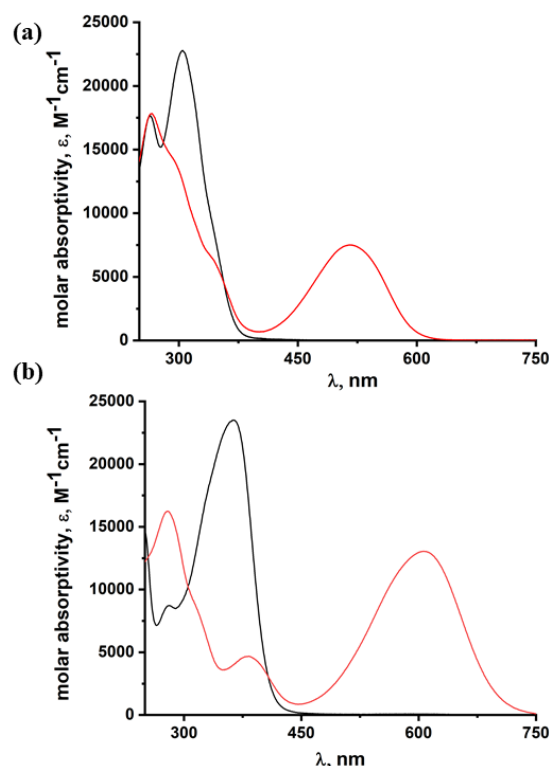


Fig. 5 Absorption spectra in CH₂Cl₂ at 298 K ($c = 2.10^{-5}$ M) of (a) **2** and (b) **[2]OTf**, before (black line) and after (red line) irradiation at 350 nm.

The electronic absorption spectrum of **2o** (Fig. 5a) shows two maxima in the UV region at 265 and 304 nm which are assigned to ¹(π - π^*) transitions. Upon UV-light irradiation (350 nm), the initial colorless solution of **2o** turns pink with the emergence of a large absorption band in the visible region centered at 514 nm, and attributed to ¹(π - π^*) transition of the closed-ring isomer (**2c**).^{40, 41} Irradiation at 525 nm of **2c**, at the photostationary state (PSS), quantitatively yields back the open form **2o**, revealing the full reversibility of the system. The open-ring form **[2o]OTf** exhibits absorption maxima at 280 and 380 nm assigned to ¹(π - π^*) and charge transfer (toward the pyridinium moiety) transitions, respectively. Similarly, UV-light irradiation of a solution of **[2o]OTf** produces the closed-ring isomer **[2c]OTf** evidenced by the appearance of the lower-lying ¹(π - π^*) transition in the visible (centered at 607 nm), and resulting in a drastic change in color, from pale yellow to dark blue (Fig. 5b). The presence of the cationic pyridinium moiety in **[2]OTf** induces a large bathochromic shift of the absorption bands relative to **2** ($\Delta\lambda_{[2]OTf/[2]} \approx 90$ nm) both in the open and closed-ring forms, due

to a reduced HOMO-LUMO gap. Relative to the normal closed-ring DTEs **1c** and **[1c]OTf**,³² the absorption spectra of the **2c** and **[2c]OTf** isomers show hypsochromic shifts ($\Delta\lambda_{1/2} \approx 50$ nm) owing to differences in the π -conjugation pathways, notably through the newly formed sp^3 carbon atom on the 2-methyl-thiophene of **2c** and **[2c]OTf** that breaks the π -electron delocalization.

Table 3 Absorption data in solution of compounds **2** and **[2]OTf**.

	$\lambda_{\text{abs}}^a/\text{nm}$ ($\epsilon/10^4\text{M}^{-1}\text{cm}^{-1}$) Open (o) forms	$\lambda_{\text{abs}}^{a,b}/\text{nm}$ Closed (c) forms (PSS)
2	265 (1.80), 304 (2.30), 345sh (0.75)	267, 297sh, 348sh, 518
[2]OTf	281 (0.87), 331 (2.33)	278, 320sh, 385, 552, 607

^a Measured in CH_2Cl_2 solution at 298 K. ^b After irradiation at 350 nm.

Monitoring the ring-closure reaction by ^1H NMR spectroscopy gives access to the percentage of conversion at the PSS. Fig. 6 shows the ^1H NMR spectra of **[2]OTf** before and after irradiation at 350 nm. The characteristic upfield shifts of the thienyl protons are observed, from 8.11 to 7.52 ppm and from 6.66 to 5.72 ppm. The central methyl groups are differently affected by the ring-closure reaction, i.e., the central 2-methyl is upfield shifted (from 2.45 to 2.10 ppm) while the central 3-methyl being downfield shifted (from 1.78 to 1.87 ppm). The PSS of **[2]OTf** has been determined to be 67 % of closed isomer, by the relative integration of the above signals between the open and the closed forms. No thermal cycloreversion has been observed in the dark for a month. The expected moderate conversion at the PSS (0.67) of **[2]OTf** is due to its 2-methyl-thiophene that increases the quantum yield of the ring-opening reaction, in comparison with the normal analogue bis-3-methyl-thiophene (PSS > 0.95).

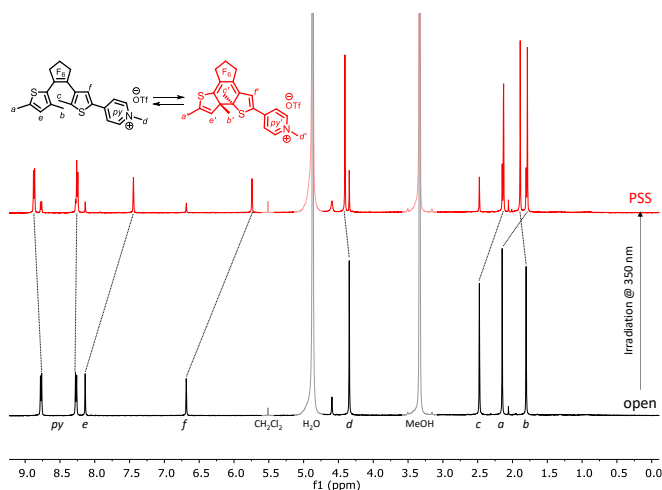


Fig. 6 ^1H NMR spectra in CD_3OD of **[2]OTf** before (bottom) and after (top) irradiation at 350 nm.

Solid-state photochromic properties

The solid-state photochromic properties of **[2]OTf**, **2-Mo₈**, **2-PW₁₂** and **1-PW₁₂** have been investigated at room temperature by diffuse reflectance spectroscopy of microcrystalline powders, and compared with those of the previously described **[1]OTf** and **1-Mo₈**.³² In this present work, **1-PMo₁₂** and **2-PMo₁₂** have been synthesized to obtain detailed crystal structures of the Keggin-type POM based assemblies, but their photochromic behaviors have not been investigated,

because the absorption properties of the $\alpha\text{-[PMo}_{12}\text{O}_{40}]^{3-}$ unit interfere with those of the DTEs (see below).

Photocyclization of **[2]OTf** upon UV irradiation at 365 nm gives rise to a drastic color change, from off white to blue, owing to the gradual growth of a new broad absorption band centered at 610 nm (Fig. 7a and Fig. S19, ESI[†]) of similar origin than recorded in solution (Fig. 5). The full width half maximum of the absorption profile in the visible is smaller for **[2]OTf** than for **[1]OTf**, on account of reduced π -delocalization. Qualitatively, the color-change effect is slower for **[2]OTf** than for **[1]OTf** (60 min for **[2]OTf** and 20 min for **[1]OTf**, to reach the PSS), which is attributed to the faster cycloreversion process of the mixed 2^+ DTE (see below), similarly as observed in solution.

Before UV irradiation, the solid-state absorption spectra of **2-Mo₈**, **2-PW₁₂** and **1-PW₁₂** (Fig. S20, ESI[†]) exhibit intense and broader absorption bands from 250 to 450 nm, attributed to both the $1(\pi\text{-}\pi^*)$ transitions of the DTE units (1o^+ or 2o^+) and the ligand-to-metal charge-transfer ($\text{O}\rightarrow\text{M}$ LMCT) transitions of the POM unit. While the absorption thresholds of **2-Mo₈** and **1-Mo₈** are well comparable with those of **[2]OTf** and **[1]OTf**, those of **1-PW₁₂** and **2-PW₁₂** are systematically red-shifted in the range 400-450 nm. The $\alpha\text{-[PW}_{12}\text{O}_{40}]^{3-}$ unit has a LMCT absorption band ($\lambda_{\text{max}} = 322$ nm) much lower in energy than that of $\beta\text{-[Mo}_8\text{O}_{26}]^{4-}$ ($\lambda_{\text{max}} = 300$ nm). Consequently, the shift of the absorption thresholds of **1-PW₁₂** and **2-PW₁₂** could be consistent with the existence of an additional absorption band, assignable to an intermolecular charge-transfer transition. This latter results in direct excitation of an electron from the HOMO of the electron-rich DTE donors into the LUMO of the electron-poor $\alpha\text{-[PW}_{12}\text{O}_{40}]^{3-}$ acceptor, in close proximity through many $\pi\text{-}\pi$ stacking interactions, which has been already observed in other charge-transfer assemblies based on Keggin-type POM units.²³

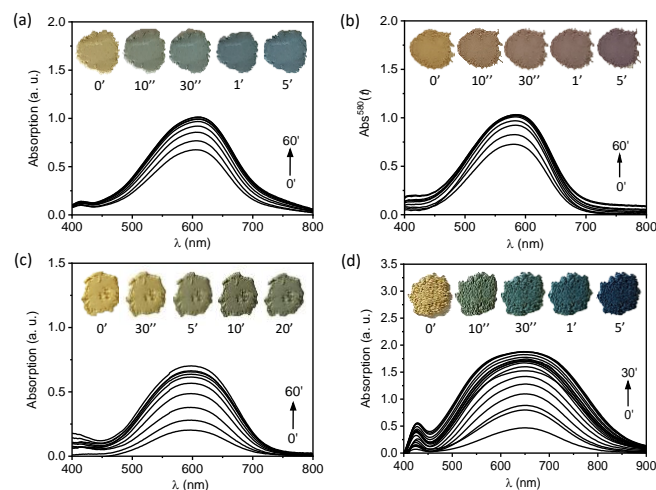


Fig. 7 Temporal evolution of the photogenerated absorption for (a) **[2]OTf**, (b) **2-Mo₈**, (c) **2-PW₁₂** and (d) **1-PW₁₂**, during UV-light irradiation (365 nm, time range of 0-60 min for **[2]OTf**, **2-Mo₈** and **2-PW₁₂**, and of 0-30 min for **1-PW₁₂**). Insets: photographs of the associated color-change effects.

As shown in Fig. 7, **2-Mo₈**, **2-PW₁₂** and **1-PW₁₂** exhibit strong solid-state photochromic properties upon UV-light irradiation ($\lambda_{\text{ex}} = 365$ nm). The color of **2-Mo₈** (Fig. 7b) and **2-PW₁₂** (Fig. 7c) shifts from off-white to purplish-blue, which slightly differs from that observed for **[2]OTf** (Fig. 7a). The photocoloration process is faster and much more pronounced for **2-Mo₈** than for **2-PW₁₂**. Upon similar UV exposure, **1-PW₁₂** gradually shifts from off-white to blue (Fig. 7d) with a high photocoloration contrast, similarly as already observed for **1-Mo₈** and **[1]OTf**.³² These color-change effects deal with the growth of broad absorption bands relative to the closed-ring isomer of the DTE units, whom the most intense is located at $\lambda_{\text{max}} = 580$ nm, 595 nm and 646 nm for **2-Mo₈**, **2-PW₁₂** and **1-PW₁₂**, respectively (Fig. 7 et Fig. S21, ESI†). All these absorption bands are blue shifted with respect to those of **[1]OTf** and **[2]OTf** ($\Delta\lambda_{\text{DTE/DTE-POM}} = 30, 24$ and 15 nm for **2-Mo₈**, **1-PW₁₂** and **2-PW₁₂**, respectively). A large blue shift of 52 nm was also observed for **1-Mo₈**,³² in well agreement with the electron-withdrawing nature of the POM units which decreases the delocalization of the π -conjugation throughout the closed-ring isomer of the DTEs, shifting its absorption at a lower wavelength. Our present work clearly evidences that the amplitude of this hypsochromic shift varies with the nature of the POM used, and is smaller for hybrid assemblies built upon the α -[PW₁₂O₄₀]³⁻ unit than for those integrating the β -[Mo₈O₂₆]⁴⁻ one. This could be explained considering that the octamolybdate anion has a smaller size and a higher negative charge, in comparison to those of α -[PM₁₂O₄₀]³⁻, leading to a higher negative charge density³⁹ which increases its electron-withdrawing character and has a stronger impact on the π -conjugation throughout the DTEs in their closed form.

Upon visible-light irradiation ($\lambda_{\text{ex}} = 590$ nm) at room temperature, the fading processes of **[2]OTf**, **2-Mo₈**, and **2-PW₁₂** rapidly occur (Fig. 8), and their pronounced coloration totally disappear in only 30 seconds, revealing highly fast reversible systems. Upon visible-light irradiation at $\lambda_{\text{ex}} = 630$ nm, the fading process of **1-PW₁₂** is slower, and the bleaching is complete after ten minutes.

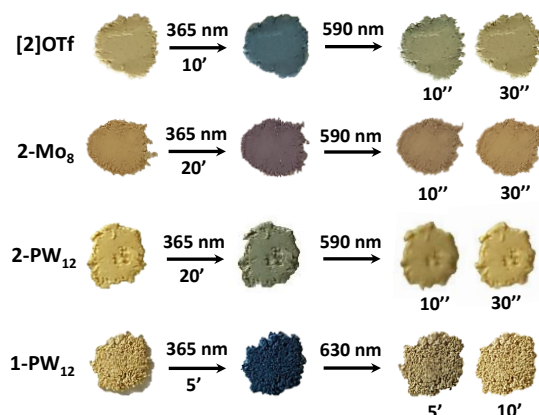


Fig. 8 Photographs of the color-change effects of **[2]OTf**, **2-Mo₈**, **2-PW₁₂** and **1-PW₁₂** at different times (in min and sec) during the coloration (upon UV-light irradiation) and fading (upon visible-light irradiation) processes.

The solid-state photocoloration and fading kinetics of **[2]OTf**, **2-Mo₈**, **2-PW₁₂** and **1-PW₁₂** have been investigated under air and at room temperature, and compared with those of **[1]OTf** and **1-Mo₈**. The coloration kinetics have been quantified by monitoring the

photogenerated absorption ($\text{Abs}^{\lambda_{\text{max}}}(t)$), at $\lambda_{\text{max}} = 610$ nm for **[2]OTf**, 595 nm for **2-PW₁₂**, 580 nm for **2-Mo₈**, and 646 nm for **1-PW₁₂**, as a function of the UV-light irradiation time (Fig. 9). The $\text{Abs}^{\lambda_{\text{max}}}(t)$ vs t plots have been satisfactorily fitted through a biexponential rate law. The color fading rates have been measured under visible light at 590 nm for **[2]OTf**, **2-Mo₈** and **2-PW₁₂**, and at 630 nm for **1-PW₁₂**, by monitoring the temporal decay of $\text{Abs}^{\lambda_{\text{max}}}(t)$ of samples once irradiated under UV excitation. Decays were fitted using a mono or a biexponential rate law. The coloration and fading kinetic parameters of all the DTE-POM assemblies together with those of **[1]OTf** and **[2]OTf** are presented in Table 4.

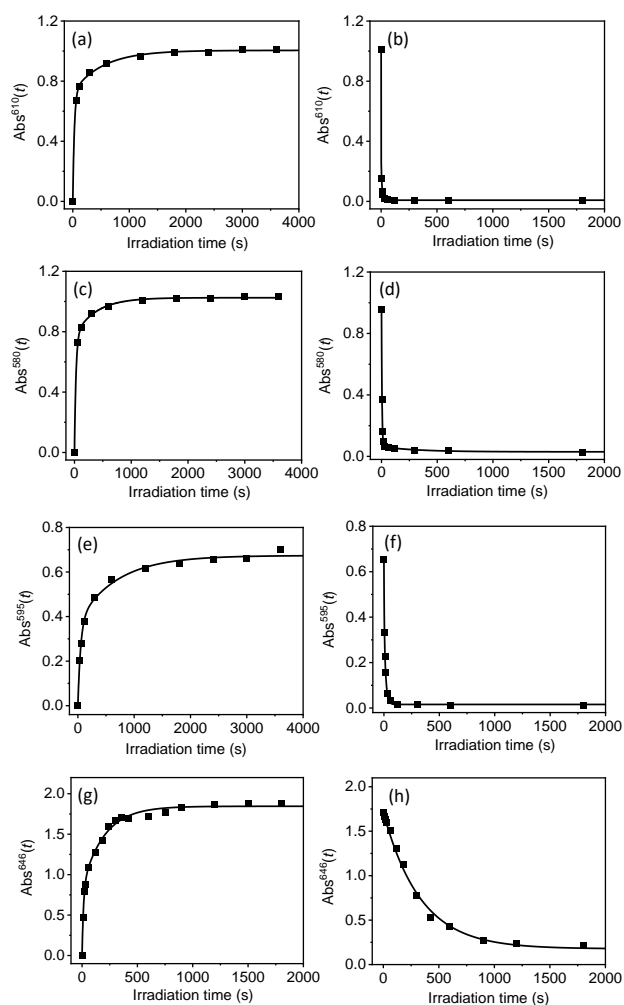


Fig. 9 Temporal Evolution of $\text{Abs}^{\lambda_{\text{max}}}(t)$ during the photocoloration and visible-light driven fading processes for **[2]OTf** (a and b), **2-Mo₈** (c and d), **2-PW₁₂**, (e and f) and **1-PW₁₂** (g and h). Black lines show the fits of the $\text{Abs}^{\lambda_{\text{max}}}(t)$ vs. t plots according to the rate laws $\text{Abs}^{\lambda_{\text{max}}}(t) = (A_1 + A_2) - A_1 \exp(-k_1 t) - A_2 \exp(-k_2 t)$ for the coloration process under UV light (365 nm), and $\text{Abs}^{\lambda_{\text{max}}}(t) = (A_0 - A_1 - A_2) + A_1 \exp(-k_1 t) + A_2 \exp(-k_2 t)$ for the fading one under visible light.

First, the photocoloration and fading rates of the compounds have been compared by considering their coloration ($t_{1/2}^c$) and fading ($t_{1/2}^f$) half-life times. Upon UV-light irradiation, **[2]OTf** exhibits a coloration rate ($t_{1/2}^c = 0.50$ min, Fig. 9a) about four-fold slower than that of **[1]OTf** ($t_{1/2}^c = 0.12$ min). However, the opposite trend is observed if considered the fading process under visible-light irradiation. The fading rate of **[2]OTf** ($t_{1/2}^f = 0.01$ min, Fig. 9b) is

considerably increased compared to that of **[1]OTf** ($t_{1/2}^f = 5.60$ min). Moreover, although the cycloreversion of the closed-ring form in **[1]OTf** is not complete,³¹ **[2]OTf** exhibits a quantitative bleaching, and noticeably, its absorption loss reaches 98% after only 30s. This is in direct accordance with previous studies on normal 3-methylthiophene and mixed 2-,3-methyl-thiophene DTEs, which revealed higher photochromic quantum yields of ring-closure reaction for normal DTEs but higher ring-opening reaction for mixed ones.⁴²

Although **1-Mo₈** and **2-Mo₈** are isostructural, the nature of the DTE strongly dictates the photoresponses of the hybrid assemblies which follow the same trend than that observed for **[1]OTf** and **[2]OTf**. The photocoloration rate of **2-Mo₈** ($t_{1/2}^c = 0.46$ min, Fig. 9c) is 4-fold slower than that of **1-Mo₈** ($t_{1/2}^c = 0.12$ min). However, its fading rate is considerably 70-fold faster (Fig. 9d), with $t_{1/2}^f = 0.05$ min and 3.50 min for **2-Mo₈** and **1-Mo₈**, respectively, and its absorption loss reaches 95% after only 2 min. The isostructural **1-PW₁₂** and **2-PW₁₂** compounds follow a similar trend. The coloration rate of **2-PW₁₂** ($t_{1/2}^c = 1.37$ min, Fig. 9e) is just over 2-fold slower than that of **1-PW₁₂** ($t_{1/2}^c = 0.60$ min, Fig. 9g). In addition, **2-PW₁₂** exhibits a completed bleaching (the absorption loss reaches 97% after 2 min), and its fading rate ($t_{1/2}^f = 0.08$ min, Fig. 9f) is 40-fold faster than that of its **1⁺** analogue ($t_{1/2}^f = 3.87$ min, Fig. 9h). These results clearly indicate that **2-Mo₈** and **2-PW₁₂** are efficient reversible photochromic systems which exhibit improved fading rates compared to **1-Mo₈** and **1-PW₁₂**.

Table 4 Photochromic kinetic parameters at room temperature of the DTE-POM assemblies, **[1]OTf** and **[2]OTf**.

Photocoloration process						
Compound	A_1^a	A_2^a	k_1^c (s ⁻¹) ^b	k_2^c (s ⁻¹) ^b	$t_{1/2}^c$ (min) ^c	R^{2d}
[1]OTf ⁴³	0.408	1.720	0.001	0.138	0.12	0.9995
1-Mo₈ ⁴³	0.391	1.790	0.015	0.123	0.12	0.9998
1-PW₁₂	1.004	0.841	0.005	0.076	0.60	0.9957
[2]OTf	0.73	0.27	0.035	0.002	0.50	0.9995
2-Mo₈	0.773	0.252	0.037	0.003	0.46	0.99966
2-PW₁₂	0.377	0.297	0.020	0.001	1.37	0.9958

Visible-light driven fading process ^e							
Compound	A_0^a	A_1^a	A_2^a	k_1^f (s ⁻¹) ^b	k_2^f (s ⁻¹) ^b	$t_{1/2}^f$ (min) ^c	R^{2d}
[1]OTf ⁴³	2.128	1.720	-	0.002	-	5.60	0.9878
1-Mo₈ ⁴³	2.181	2.118	-	0.003	-	3.50	0.9822
1-PW₁₂	1.714	1.537	-	0.003	-	3.87	0.9974
[2]OTf	1.01	0.899	0.108	0.533	0.066	0.01	0.9999
2-Mo₈	0.959	0.896	0.033	0.215	0.003	0.05	0.9999
2-PW₁₂	0.654	0.238	0.400	0.382	0.068	0.08	0.9996

^aThe $Abs^{2,max}(t)$ vs t plots were fitted as $Abs^{2,max}(t) = (A_1 + A_2) - A_1 \exp(-k_1^c t) - A_2 \exp(-k_2^c t)$ for the coloration process and as $Abs^{2,max}(t) = (A_0 - A_1 - A_2) + A_1 \exp(-k_1^f t) + A_2 \exp(-k_2^f t)$ for the fading ones. ^bColoration (k^c) and fading (k^f) rate constants. ^cFor the coloration process, the half-life time $t_{1/2}^c$ is defined as the UV irradiation time required for $Abs^{2,max}(t)$ to reach half of its maximum value. For the fading ones, $t_{1/2}^f$ is defined as the irradiation time required for $Abs^{2,max}(t)$ to reach the $A_0 - (A_1 + A_2)/2$ value. ^dRegression coefficient for the $Abs^{2,max}(t)$ vs t plot. ^e $\lambda_{exc} = 590$ nm for **[2]OTf** and **2-PW₁₂**; $\lambda_{exc} = 630$ nm for **1-PW₁₂**.

For a given DTE, the UV-induced coloration processes of the hybrid assemblies are significantly impacted by the nature of the POM unit. Indeed, the coloration rates of **2-Mo₈** ($t_{1/2}^c = 0.46$ min) is as fast as that of **[2]OTf** ($t_{1/2}^c = 0.50$ min), and a similar trend was observed for **1-Mo₈** ($t_{1/2}^c = 0.12$ min) and **[1]OTf** ($t_{1/2}^c = 0.12$ min). Thus, the photocyclization processes of **1⁺** and **2⁺** are not disturbed by their assembling with the β -[Mo₈O₂₆]⁴⁻ unit. In contrast, the coloration rates of **2-PW₁₂** ($t_{1/2}^c = 1.37$ min) and **1-PW₁₂** ($t_{1/2}^c = 0.60$ min) are slower than those of **[1]OTf** and **[2]OTf**, revealing that the coupling of the DTEs with the α -[PW₁₂O₄₀]³⁻ unit slightly affects the efficiency of the photocyclization processes. This is in direct line with the energy of the LMCT transitions of the POM units which decreases in the trend β -[Mo₈O₂₆]⁴⁻ > α -[PW₁₂O₄₀]³⁻ > α -[PMo₁₂O₄₀]³⁻ (Fig. S22, ESI[†]). The low-energy LMCT transitions of the α -[PW₁₂O₄₀]³⁻ polyanion strongly overlap the absorption bands of the DTEs in the range 300-350 nm, and thus, the POM dramatically competes to absorb the excitation UV energy needed to activate their ring-closure process. This competition is even more marked in hybrid assemblies built upon the α -[PMo₁₂O₄₀]³⁻ entity, which explains why their poor photochromic properties have not been considered in our present work. In marked contrast, the fading rate of **2-Mo₈** upon visible light irradiation ($t_{1/2}^f = 0.05$ min) is well comparable with that of **2-PW₁₂** ($t_{1/2}^f = 0.08$ min), and a similar trend is observed for **1-Mo₈** ($t_{1/2}^f = 3.50$ min) and **1-PW₁₂** ($t_{1/2}^f = 3.87$ min). This evidences that the back cycloreversion process of the DTEs is not significantly impacted by the POMs, essentially because both the β -[Mo₈O₂₆]⁴⁻ and α -[PW₁₂O₄₀]³⁻ units have large transparency windows in the range 400-800 nm.

Our complete kinetics study finds that within this new series, **2-Mo₈** is the most efficient photochromic hybrid POM-DTE system, which combines fast coloration rate, high coloration contrast, and very fast and complete fading process. Thus, its robustness for repeatable "recording-erasing" processes at room temperature was investigated by monitoring the evolution of the absorption at 580 nm of a sample alternatively irradiated for 20 secs with UV light (365 nm), and then for 1 min with visible light (590 nm) (Fig. 10). **2-Mo₈** exhibits a high cyclability on sixty coloration/fading cycles (n), with only a very limited photofatigue. The empirical linear evolution of the $Abs^{580}(n)$ vs. n plot allows predicting that the color-change effect should disappear at the end of about 1500 cycles.

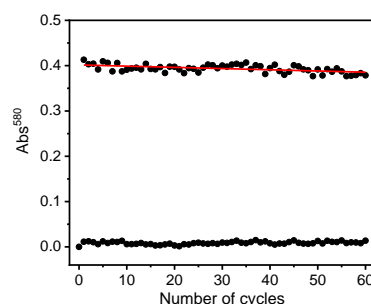


Fig. 10 Evolution of the absorbance monitored at 580 nm for **2-Mo₈** during successive coloration/bleach cycles (n). The solid red line corresponds to the empirical linear fit of the $Abs^{580}(n)$ vs. n according to the relationships $Abs^{580}(n) = -2.680 \cdot 10^{-4}n + 0.402$.

Conclusion

Five new photochromic supramolecular assemblies which combine a normal (**1**⁺) or a mixed (**2**⁺) cationic dithienylethene (DTE) with three different POM units have been successfully prepared. This study completes well our recent work devoted to (1)₄[Mo₈O₂₆]-4DMF (**1-Mo₈**), the very first member of this DTE-POM series. All these hybrid materials show a high degree of organization, conducive to the establishment of structure-properties relationships. The (1)₃[PM₁₂O₄₀]-5ACN (M = W, Mo) (**1-PW₁₂** and **1-PMo₁₂**) and (2)₃[PM₁₂O₄₀]-5ACN (M = W, Mo) (**2-PW₁₂** and **2-PMo₁₂**) compounds are isostructural, while the crystal packing of (2)₄[Mo₈O₂₆]-4DMF (**2-Mo₈**) is strictly similar to that of **1-Mo₈**. Combined X-ray crystallographic and spectroscopic analyses have enabled to highlight the precise impact of both DTEs and POMs on the photochromic properties of the assemblies, as well as synergistic effects between the organic and inorganic components. Noticeably, the presence of the POMs significantly modifies the photoresponses of **1**⁺ and **2**⁺ in the solid-state. Upon UV-light irradiation, the absorption of their closed-ring isomer undergoes a blue shift which increases with the electron-withdrawing character of the POMs, and is more pronounced for β-[Mo₈O₂₆]⁴⁻ than for α-[PW₁₂O₄₀]³⁻. The photocyclization process of the DTEs also varies with the nature of the POM used. The beneficial association of **1**⁺ and **2**⁺ with β-[Mo₈O₂₆]⁴⁻ which has a high energy LMCT transitions prevents a strong competition between both organic and inorganic components to absorb the excitation UV energy, that causes a decrease of the photocolouration rates, as observed in POM-DTE assemblies built upon the α-[PM₁₂O₄₀]³⁻ (M = W, Mo) unit. In addition, upon visible-light excitation, **2-Mo₈** and **2-PW₁₂** exhibit complete bleaching with cycloreversion rates faster than those of their **1**⁺ counterparts. In particular, **2-Mo₈** exhibits remarkable photochromic properties at room temperature, which include a marked photocolouration contrast, fast photoswitching processes, and a high cyclability. **2-Mo₈** stands as the most efficient system for fast and complete fading process among hybrid photochrome-based POM assemblies. Thus, this strategy of assembling allows transferring the photoswitching efficiency of mixed DTEs from the solution to the solid state, and it opens the way towards the design of novel robust photoresponsive materials with improved fading processes and high light-driven “recording–erasing” potential.

Acknowledgements

This work was supported by the CNRS, the Université de Nantes, the Université de Rennes 1, the Université Bretagne Loire, the Ministère de l'Enseignement Supérieur et de la Recherche, and the LUMOMAT project supported by the Région des Pays de la Loire. Thierry Roisnel is gratefully acknowledged for help with X-ray analysis of **2** and **[2]OTf**.

Conflicts of interest

There are no conflicts to declare.

References

1. A. Sartorel, M. Bonchio, S. Campagna and F. Scandola, *Chem. Soc. Rev.*, 2013, **42**, 2262-2280.
2. S.-S. Wang and G.-Y. Yang, *Chem. Rev.*, 2015, **115**, 4893-4962.
3. K. Narasimhan, S. Pillay, N. R. Bin Ahmad, Z. Bikadi, E. Hazai, L. Yan, P. R. Kolatkar, K. Pervushin and R. Jauch, *ACS Chem. Biol.*, 2011, **6**, 573-581.
4. B. Č. Mirjana, L. Milan, L. Jovana, S. M. Ali, K. Ulrich and Z. K. Danijela, *Curr. Med. Chem.*, 2020, **27**, 362-379.
5. J. M. Clemente-Juan, E. Coronado and A. Gaita-Ariño, *Chem. Soc. Rev.*, 2012, **41**, 7464-7478.
6. A. Dolbecq, E. Dumas, C. R. Mayer and P. Mialane, *Chem. Rev.*, 2010, **110**, 6009-6048.
7. A. Saad, O. Oms, J. Marrot, A. Dolbecq, K. Hakouk, H. El Bekkachi, S. Jobic, P. Deniard, R. Dessapt, D. Garrot, K. Boukhedaden, R. Liu, G. Zhang, B. Keita and P. Mialane, *J. Mater. Chem. C*, 2014, **2**, 4748-4758.
8. Y.-F. Song and R. Tsunashima, *Chem. Soc. Rev.*, 2012, **41**, 7384-7402.
9. A. Proust, B. Matt, R. Villanneau, G. Guillemot, P. Gouzerh and G. Izzet, *Chem. Soc. Rev.*, 2012, **41**, 7605-7622.
10. M.-S. Wang, G. Xu, Z.-J. Zhang and G.-C. Guo, *Chem. Comm.*, 2010, **46**, 361-376.
11. R. Dessapt, M. Collet, V. Coué, M. Bujoli-Doeuff, S. Jobic, C. Lee and M.-H. Whangbo, *Inorg. Chem.*, 2009, **48**, 574-580.
12. T. Yamase, *Chem. Rev.*, 1998, **98**, 307-326.
13. W. Zou, A. González, D. Jampaiah, R. Ramanathan, M. Taha, S. Walia, S. Sriram, M. Bhaskaran, J. M. Dominguez-Vera and V. Bansal, *Nat. Comm.*, 2018, **9**, 3743.
14. Y. Yang, J. Li, X. Li, L. Guan, Z. Gao, L. Duan, F. Jia and G. Gao, *ACS Appl. Mater. Interfaces*, 2019, **11**, 14322-14328.
15. N. Sun, A. Wu, Y. Yu, X. Gao and L. Zheng, *Chem.-Eur. J.*, 2019, **25**, 6203-6211.
16. X. Chen, X. Zhu, S.-R. Zhang, J. Pan, P. Huang, C. Zhang, G. Ding, Y. Zhou, K. Zhou, V. A. L. Roy and S.-T. Han, *Adv. Mater. Technol.*, 2019, **4**, 1800551.
17. C. Kato, R. Machida, R. Maruyama, R. Tsunashima, X.-M. Ren, M. Kurmoo, K. Inoue and S. Nishihara, *Angew. Chem. Int. Ed.*, 2018, **57**, 13429-13432.
18. K. Hakouk, O. Oms, A. Dolbecq, H. El Moll, J. Marrot, M. Evain, F. Molton, C. Duboc, P. Deniard, S. Jobic, P. Mialane and R. Dessapt, *Inorg. Chem.*, 2013, **52**, 555-557.
19. O. Oms, K. Hakouk, R. Dessapt, P. Deniard, S. Jobic, A. Dolbecq, T. Palacin, L. Nadjo, B. Keita, J. Marrot and P. Mialane, *Chem. Comm.*, 2012, **48**, 12103-12105.
20. A. Parrot, G. Izzet, L.-M. Chamoreau, A. Proust, O. Oms, A. Dolbecq, K. Hakouk, H. El Bekkachi, P. Deniard, R. Dessapt and P. Mialane, *Inorg. Chem.*, 2013, **52**, 11156-11163.
21. Z. Li, G. Wang, Y. Ye, B. Li, H. Li and B. Chen, *Angew. Chem. Int. Ed.*, 2019, **58**, 18025-18031.
22. J.-D. Compain, P. Deniard, R. Dessapt, A. Dolbecq, O. Oms, F. Sécheresse, J. Marrot and P. Mialane, *Chem. Comm.*, 2010, **46**, 7733-7735.
23. K. Hakouk, O. Oms, A. Dolbecq, J. Marrot, A. Saad, P. Mialane, H. El Bekkachi, S. Jobic, P. Deniard and R. Dessapt, *J. Mater. Chem. C*, 2014, **2**, 1628-1641.
24. M. Irie, T. Fukaminato, K. Matsuda and S. Kobatake, *Chem. Rev.*, 2014, **114**, 12174-12277.

25. Z. Li, H. Chen, B. Li, Y. Xie, X. Gong, X. Liu, H. Li and Y. Zhao, *Adv. Sci.*, 2019, **6**, 1901529.
26. F. Meng, Y.-M. Hervault, Q. Shao, B. Hu, L. Norel, S. Rigaut and X. Chen, *Nat. Comm.*, 2014, **5**, 3023.
27. C. Jia, A. Migliore, N. Xin, S. Huang, J. Wang, Q. Yang, S. Wang, H. Chen, D. Wang, B. Feng, Z. Liu, G. Zhang, D.-H. Qu, H. Tian, M. A. Ratner, H. Q. Xu, A. Nitzan and X. Guo, *Science*, 2016, **352**, 1443.
28. J. Boixel, V. Guerchais, H. Le Bozec, D. Jacquemin, A. Amar, A. Boucekkine, A. Colombo, C. Dragonetti, D. Marinotto, D. Roberto, S. Righetto and R. De Angelis, *J. Am. Chem. Soc.*, 2014, **136**, 5367-5375.
29. H. Zhao, E. Garoni, T. Roisnel, A. Colombo, C. Dragonetti, D. Marinotto, S. Righetto, D. Roberto, D. Jacquemin, J. Boixel and V. Guerchais, *Inorg. Chem*, 2018, **57**, 7051-7063.
30. M. Hojorat, H. Al Sabea, L. Norel, K. Bernot, T. Roisnel, F. Gendron, B. L. Guennic, E. Trzop, E. Collet, J. R. Long and S. Rigaut, *J. Am. Chem. Soc.*, 2020, **142**, 931-936.
31. D. Majee and S. Presolski, *ACS Catalysis*, 2021, **11**, 2244-2252.
32. P. Bolle, C. Menet, M. Puget, H. Serier-Brault, S. Katao, V. Guerchais, F. Boucher, T. Kawai, J. Boixel and R. Dessapt, *J. Mater. Chem. C*, 2021, **9**, 13072-13076.
33. K. Uchida and M. Irie, *ChemInform*, 1996, **27**.
34. S. L. Gilat, S. H. Kawai and J.-M. Lehn, *J. Chem. Soc. Chem. Comm.*, 1993, 1439-1442.
35. H. D. Samachetty, V. Lemieux and N. R. Branda, *Tetrahedron*, 2008, **64**, 8292-8300.
36. F. Sun, F. Zhang, H. Guo, X. Zhou, R. Wang and F. Zhao, *Tetrahedron*, 2003, **59**, 7615-7621.
37. A. J. Bridgeman, *Chem. Phys.*, 2003, **287**, 55-69.
38. C. Rocchiccioli-Deltcheff, M. Fournier, R. Franck and R. Thouvenot, *Inorg. Chem*, 1983, **22**, 207-216.
39. A. Misra, K. Kozma, C. Streb and M. Nyman, *Angew. Chem. Int. Ed.*, 2020, **59**, 596-612.
40. T. C. Pijper, T. Kudernac, W. R. Browne and B. L. Feringa, *J. Phys. Chem. C*, 2013, **117**, 17623-17632.
41. U. Kingo and I. Masahiro, *Chem. Lett.*, 1995, **24**, 969-970.
42. K. Uchida and M. Irie, *Chem. Lett.*, 1995, **24**, 969-970.